AN ABSTRACT OF THE THESIS OF

Ashley N. Ellenson for the degree of Master of Science in Civil Engineering presented on July 7, 2017.

Title: Weather and Large Waves along the Oregon Coast: Atmospheric Controls on a Numerical Wave Model

Abstract approved: _____

H. Tuba Özkan-Haller

In this study, the effects of implementing different wind input or physics packages in a numerical wave model to recreate large wave conditions are explored. Three large wave events are simulated with WaveWatch III. The wind inputs which are compared are NCEP's Global Forecasting System (GFS) with 0.5° resolution and Climate Forecast System Reanalysis (CFSR) with 0.312° resolution, and the physics packages which are compared are ST2 (Tolman and Chalikov, 1996) and ST4 (Ardhuin et al, 2010). The modelled output, including spectral shape and bulk parameter time series, are compared with National Data Buoy Center buoy observations offshore of Newport, OR. The atmospheric conditions which generate these large waves include a wind feature called a coastal jet along with a distant cyclone. The energetic contribution of these simultaneously occurring atmospheric features results in a wave field characterized by bi-modal energy spectra for two

events and uni-modal energy spectra for the third event. The analysis of model output includes evaluates bulk parameter time series significant wave height, mean period and mean wave direction derived from partitioned energy spectra. A consistent underestimation in wave energy emanating from the southwestern direction is found for the output associated with all model configurations. This wave energy is generated by the coastal jet. An overestimation in swell energy emanating from the northwest is also found for all model configurations. The model configuration which features the combination of CFSR winds with Ardhuin et al (2010) physics results in the best performance for the largest wave heights, with a reduction in error for overall bulk parameters as well as partitioned bulk parameters.

Weather and Large Waves along the Oregon Coast: Atmospheric
Controls on a Numerical Wave Model

by

Ashley N. Ellenson

A THESIS

submitted to

Oregon State University

in partial fulfillment of
the requirements for the
degree of

Master of Science

Presented July 7, 2017
Commencement June 2018

Master of Science thesis of Ashley N. Ellenson presented on July 7, 2017.

APPROVED:

_____

Major Professor, representing Civil Engineering

_____

Jason Weiss Head of the Civil and Construction Engineering of Engineering

_____

Dean of the Graduate School

_____

Ashley N. Ellenson, Author

ACKNOWLEDGEMENTS

I would like to acknowledge my committee members, H. Tuba Özkan-Haller, Jim Thomson, and Merrick Haller for their guidance in helping me become a thoughtful scholar and put together this work. Thanks to Gabriel García-Medina for his availability, technical help and enlightening advice. I also would like to express gratitude to all of my friends within the department for their support and invaluable friendships. Thanks to my family for always keeping me grounded and loved. Finally, thanks to the cold and foggy Oregon ocean for the constant inspiration.

TABLE OF CONTENTS

LIST OF FIGURES

LIST OF TABLES

LIST OF APPENDIX FIGURES

LIST OF APPENDIX TABLES

Chapter 1   Introduction

Large wave heights pose dangers to those engaging in maritime activities, physical risk to coastal infrastructure, and hazards to residents and recreational beach users. A system that can accurately predict such sea states is important for quantifying the risk associated with large wave events. This system would provide an accurate characterization of a large wave event by producing information about bulk parameters such as wave height, wave period, and mean wave direction, or more detailed quantities such as directional wave spectra. Model output in the form of forecasts and hindcasts can be utilized in different ways to benefit hazard mitigation efforts which seek to avoid financial losses and damage to infrastructure. The predictive capacity of a forecast can provide people with timely information which can guide emergency response procedures, while hindcasts provide information about the regional wave climate, which can help communities develop appropriate coastal management policies. To increase the accuracy of such prediction systems, detailed comparisons of model output and observations can be analyzed. Disagreements between the two provide opportunities to learn more about the environmental context surrounding modelling deficiencies. This knowledge can result in more accurate quantification and communication of forecast uncertainty. Further, newfound understanding of model error can provide opportunities to improve the modeling system by providing information about conditions when models fail.

The U.S. Pacific Northwest is an environment subject to large wave events at approximately the rate of one 10 meter wave height event per year. The strongest storms produce wave heights of 14-15 m [16]. Studies have shown that the average annual wave height has been increasing throughout the past quarter century, and the largest wave heights are increasing at a more rapid rate than that of the average wave height [16, 15, 1, 18]. This makes the U.S. Pacific Northwest an ideal location for evaluating the performance of a forecasting tool for predicting large wave events.

Spectral wave propagation models are the standard tool for producing wave forecasts, and their output is sensitive to input variables, such as the wind forcing or parameterizations of physical processes. Simulations that utilize different combinations of wind input and model physics can lead to a greater understanding of the primary drivers of an event or ensure that the model delivers reasonable results [4, 13]. Studies to date suggest that a more accurate wind input will yield a more accurate wave model output [6, 5, 13], and that there is a need for improved parameterizations of the energy exchange between the wind and wave fields [2, 14].

In this study, we utilize a hindcast of wave conditions that was performed for the coasts of Oregon and Southwest Washington using a spectral wave propagation model [8]. The hindcast, originally carried out for applications within the renewable energy sector, provides information on the spatial and temporal variability of the wavefield along the coastline. Herein, reductions in overall and partitioned bulk parameter error are made in hindcast of events associated with large wave events where wave heights exceed 6 m. Our methodology includes simulating sev-

eral large wave events with a variety of model configurations. The hourly time series of bulk parameter and wave spectra produced by these model configurations are studied in conjunction with the atmospheric forcing throughout the event. We then correlate specific atmospheric forcing features to observed model deficiencies. Comparison of spectral output between each model configuration then reveals how modelling improvements occur.

We begin with a description of the typical atmospheric conditions, specific to the Northeast Pacific Ocean, leading to a large wave event. Three historical large wave events are simulated, and are described in Section 1.2. Section 2 then describes the wave model components wind input and physics packages. Permutations of these components are then implemented in four different model configurations. The modelled output is compared with buoy observations of the events in Section 3. This analysis includes consideration of bulk parameter and frequency-direction energy spectra comparisons. In Section 4, the importance of the temporal and spatial resolution of the model components is explored by varying the resolution of these components in three additional simulations of a large wave event.

1.1   Atmospheric Forcing of Large Wave Events in the Pacific Northwest

The waves associated with large wave events can range from long period swell energy to short-period wind sea energy. Waves arriving at the Pacific NW (PNW)

voastline are often generated by mid-latitude cyclones. While cyclones exist throughout the Pacific Ocean, the strongest cyclones originate east of Japan and south of Alaska. After cyclogenesis, they travel several thousands of miles east and decay as they travel north. They often pass over the PNW coastline, and ultimate dissipation usually happens north of $50°$ [9, 10, 12]. This sequence can last several days, and pressures can drop 20-30 mbars [9]. The wave energy associated with the life cycle of a cyclone can take on several forms. The wave energy generated as the cyclone first develops will arrive at the PNW coastline as long period swell. As the cyclone moves closer to the region, the wave energy will be characterized by periods that are shorter than the original incoming swell energy. The shortest wave periods are generated locally ($\sim$4-7s), and the intermediate to long wave periods ($\sim$8-20s) are generated when the cyclone is at a further distance from land.

In addition to cyclones, atmospheric fronts can also generate wave energy. As a front that is obliquely oriented relative to the shoreline travels landward, low-level blocking may occur. The air flow preceding the front, which would usually travel cross-mountain, is directed upward along this stable region. It then veers cross-mountain intensely as it travels inland over the stable region and coastal range. This introduces pressure perturbations which are not alongshore uniform. The combination of the low-level blocking and longshore pressure variations induces a narrow, strong, southerly wind called a "coastal boundary jet," which is tightly bound to the shore. Along the PNW coastline, it can extend from the California-Oregon border to Vancouver Island and reach speeds greater than 25 m/s. [7].
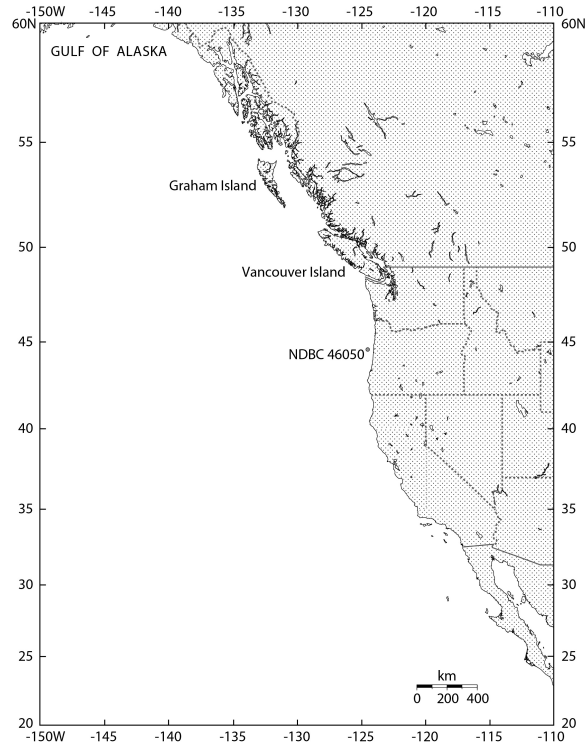
Figure 1.1: The region of interest.

The results of an atmospheric modelling study found that the feature decays longitudinally, or cross-shore, five times more quickly than latitudinally, or along-shore [7]. The repercussion of this jet in wave energy is a strong wind signal from the south which can be associated with very short (4 s) to intermediate ($\sim$10 s) periods depending on the duration of the jet and the fetch it encompasses. The atmospheric forcing of the events analyzed in this study feature the coastal jet either primarily or in conjunction with a mid-latitude cyclone, described further in Section 1.2. The relative influence of the two atmospheric features on wave energy is observed in the resulting energy spectra. These are analyzed further in Section

3.

1.2   Case Studies

Inspection of the hindcast by Garcia et al (2014) shows that the original model performs poorly in terms of absolute error for events where wave heights exceeded 6 m (see Appendix A) [8] . Specifically, when the hindcast output was divided into bins of significant wave height smaller than 4 m and larger than 6 m, root-mean-squared-error (RMSE) was increased from 0.42 m to 1.34 meter, and bias was switched from an overestimation of 0.14 m to an underestimation of 0.67 m. (Error metrics RMSE and bias are defined as in Garcia et al (2014) and are reproduced in Appendix A). We searched for large wave events, which were defined as $H_s \geq$ 6 m for at least 5 hours, from the time series of three years (2009-2011) of model output. We identified approximately 12 such events, and inspected these to find when the model performed particularly poorly. We found that 9 out of the 12 events featured the coastal jet as described in Section 1.1 either before or during the peak wave height of the event time series. Three of these storms were selected to serve as case studies for hindcast improvement and are summarized in Table 1.1. Time series of significant wave height, H_s, mean period, T_m, mean wave direction, MWD, wind direction and wind speed are presented in Figure 1.2.

These three events are described further as follows. First, the atmospheric conditions preceding and during the event are described. Then the observations of H_s, T_m, MWD at NDBC buoy 46050 are discussed. MWD is defined in a nautical
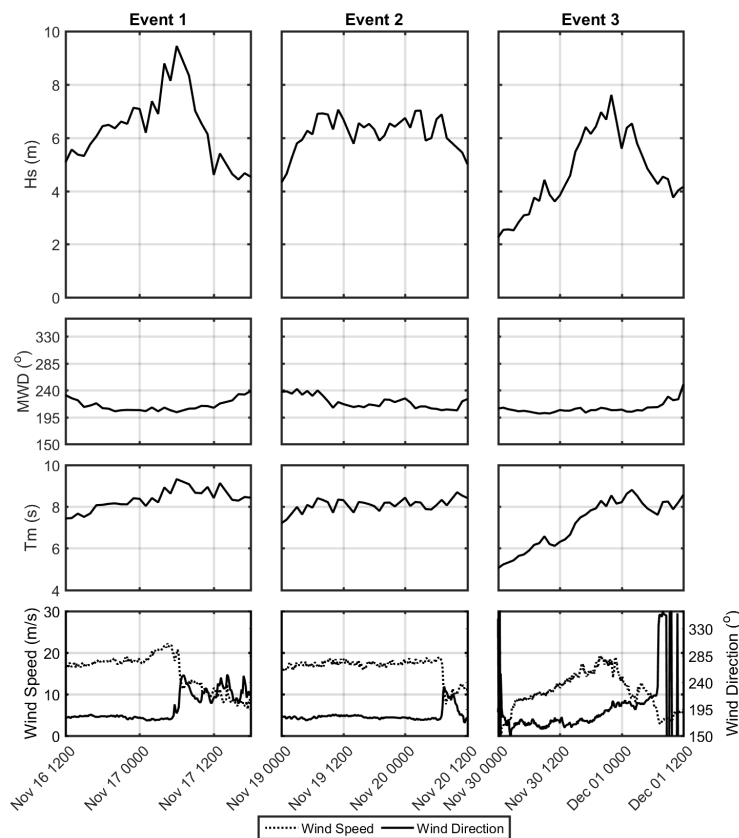
Figure 1.2: The H_s, MWD, T_m, wind speed and wind direction as observed by NDBC buoy 46050.

convention, where 0° indicates waves incident from the north, 90° from the east, 180° from the south, and 270° from the west. The description of the events will focus on the atmospheric features of the NE Pacific and their locations relative to NDBC buoy 46050 (see Figure 1.1). This buoy is located roughly in the middle of the PNW coastline 23 miles west of Newport, OR in 137 m water depth.

1.2.1   Event 1

The first selected event begins on November 16, 2009 at 1200, when a low pressure center at 980 mb is located on Graham Island and a southerly coastal jet extends from the California-Oregon border to the Washington-Canada border. The low remains at approximately 980 mb and on Graham Island until November 16, at 2000 hours, at which point the low pressure system dissipates. The coastal jet slowly decreases in extent during this time, with its final and shortest extent spanning from the CA-OR border to NDBC buoy 46050. A few hours later, on November 17, at 0000 hours, another low pressure system at approximately 990 mb forms approximately 700 km NW of NDBC buoy 46050. This low pressure system slowly tracks northeast as the coastal jet wind speed strengthens to over 25 m/s and increases in latitudinal extent. A third, smaller low pressure center at 990 mb forms by November 17, 0400, 400 km NNW of NDBC buoy 46050. At this point, the coastal jet extends along the entire Washington and Oregon coastline (see Figure 1.3) and reaches wind speeds greater than 25 m/s. The storm has tracked over land by November 17, 0900. The low pressure centers coalesce and move towards Vancouver Island, and the coastal jet weakens and ceases to exist by November 17, 1000.

Local conditions at NDBC buoy 46050 begin with an H_s of 5 m, a MWD of approximately 230° and a T_m of 7.5 s. The wind is southerly, coming from 180° at a speed of 15 m/s. As the H_s grows, the T_m increases and the MWD becomes aligned with the wind. Concurrently, the wind remains southerly and increases in

speed, reaching just over 20 m/s at its peak wind speed. The increase in wind speed coincides with the most intense coastal jet of the time series at November 17, 0400, and as pictured in Figure 1.3. After the low pressure systems coalesce and travel over Vancouver Island, the local wind drops rapidly and changes direction. It is at this point that the H_s reaches a maximum of approximately 9 m at November 17, 0600. At the H_s maximum, MWD is from approximately 210°, and T_m at 9 s. After the event peak, H_s declines quickly and the MWD reaches 240° by the end of the time series. T_m remains at approximately 9 s throughout this time.

1.2.2   Event 2

As opposed to Event 1, this event is characterized by a weaker coastal jet signal; the coastal jet dissipates almost entirely and then is regenerated with lesser intensity and smaller latitudinal extent than the jet associated with Event 1. The event begins with a low pressure system of 970 mbar focused on Graham Island and southerly winds extending from the OR-CA border to Vancouver Island at November 19, 2009 at 0000 hours. The coastal jet dissipates as the low pressure system travels north (see Figure 1.4), and traces of it exist only along the central Oregon coast by November 19, 1400. The jet then strengthens in wind speed and grows in latitudinal extent by November 19, 2100, associated with a low pressure system situated approximately 400 km NW of NDBC buoy 46050. At its maximum extent, the jet spans the entire Oregon coastline and part of the southern Washington coast, and wind speeds reach between 20-25 m/s. As the low pressure

system slides over Vancouver Island, the jet decreases appreciably in strength and size by November 20, 1000.

In contrast to the H_s associated with Events 1 and 3, which increase and decrease rapidly, H_s associated with Event 2 is sustained at a relatively constant level for approximately 24 hours. Wave conditions at NDBC buoy 46050 (see Figure 1.2) begin with an H_s of approximately 4.5 m, a MWD coming from the WSW at 240°, and a T_m of approximately 7.5 s. The wind signal begins southerly at 180° and at a speed of approximately 18 m/s. As H_s increases to exceed 6 m within 6 hours, the MWD decreases to indicate wave energy incident from a more southern direction, reaching 220°, and the T_m increases slightly to approximately 8 s. For the remainder of the event, the bulk parameters remain at these values, approximately 6-7 m for H_s, 200°-220° for MWD, and 8 s for T_m. The wind remains southerly at approximately 18 m/s during the entire event. The decrease and direction change of the wind coincides with a decrease in H_s at the end of the event.

1.2.3 Event 3

As opposed to the cyclones of Events 1 and 2, which are situated between 400 - 1200 km from NDBC buoy 46050, the cyclone of Event 3 is further away, situated at an additional 1000 km northwest of Graham Island. The event begins on November 30, 2010 at 0000 hours, with the low pressure system at 980 mbar in the Gulf of Alaska. As the low pressure center tightens, a coastal jet forms by 0700

hours, extending from Vancouver Island to the OR-CA border (see Figure 1.5). The southerly wind reaches speeds of 20 m/s. The low pressure system travels southeast towards Graham Island as the coastal jet tightens longitudinally, originally spanning 3° at 800 hrs to less than a degree by 2000 hrs. The coastal jet feature also translates south, extending to NDBC buoy 46050 from the CA-OR border before dissipating entirely.

The third event is similar to Event 1 in that H_s grows substantially to reach a maximum over the course of several hours. However, unlike Events 1 and 2, the T_m and wind also grow substantially as opposed to remaining consistent throughout the event. Wave conditions begin with H_s at 2.5 m, T_m of 5 s, and MWD at approximately 210°. The windspeed is at 5 m/s and is southerly, at 180°, at this point. As H_s grows to reach 7.5 m in 18 hours, T_m and windspeed also grow to reach 8 s and almost 20 m/s at the H_s peak (see Figure 1.2). The increase in these parameters coincides with the southward translation of the coastal jet. The MWD remains entirely from the south at 220° throughout the event. After the H_s peak, both the windspeed and H_s decrease dramatically, while T_m increases slightly to 9 s, and MWD remains from the south.

Table 1.1: Events Summary

Event	Start Date	Max Hs (m)	Avg MWD (°)	Avg T_m (s)	Avg Wind-speed (m/s)	Avg Wind Direction (°)	Atmospheric Description
1	11/16/09	9.4	221	8.4	15	198	Rapid increase in wave height Strong coastal jet 3 cyclones: (1) at Graham Island and (2) occur simultaneously within 700 km NW of NDBC buoy 46050
2	11/19/09	7.0	220	8.1	16	184	Consistent wave height Jet disappears and reappears, of smaller latitudinal extent and lesser intensity 2 cyclones: (1) at Graham Island and (1) 400 km NW of NDBC buoy 46050
3	11/30/10	7.6	210	7.2	11	181	Rapid increase in wave height Jet translates south along the coast 1 Cyclone: (1) in the Gulf of Alaska
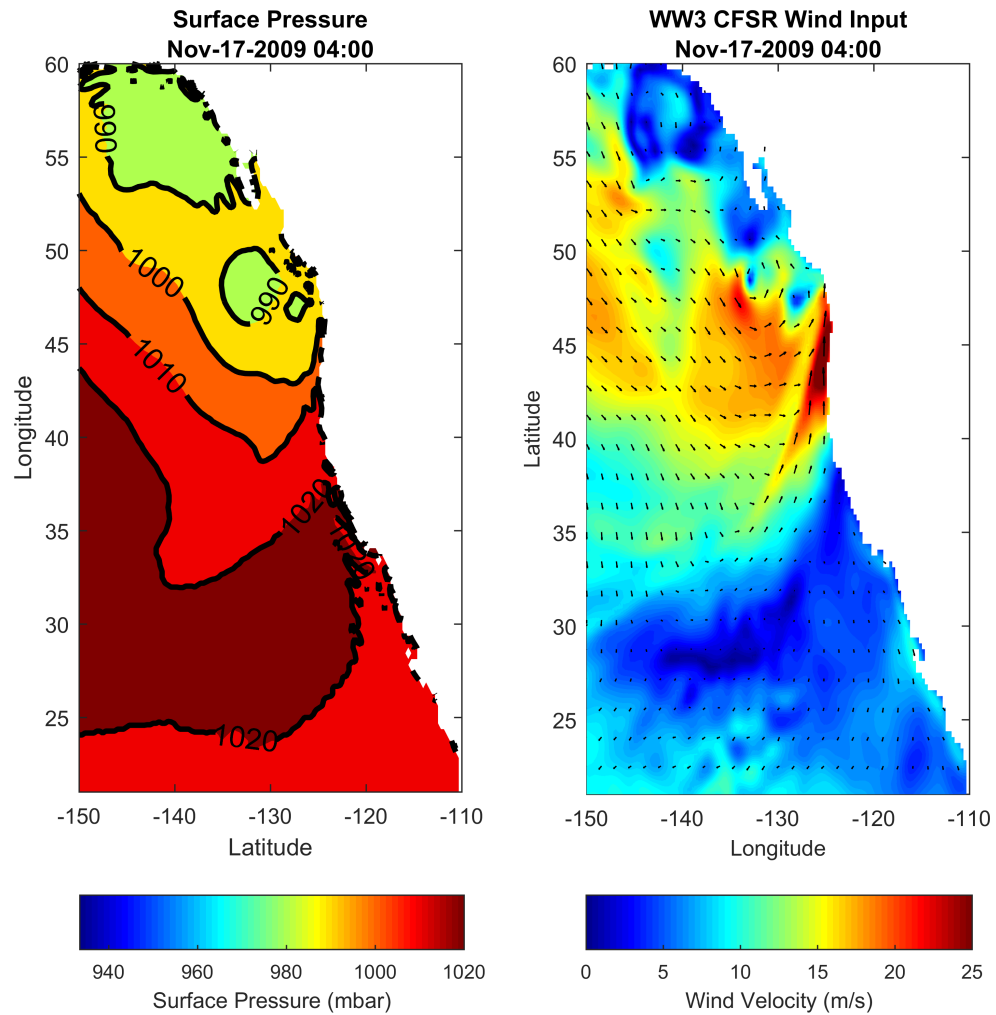
Figure 1.3: The surface pressure and 10 m wind forcing during the peak H_s hour of Event 1. The colors are wind magnitude and contours are pressure in mbar.
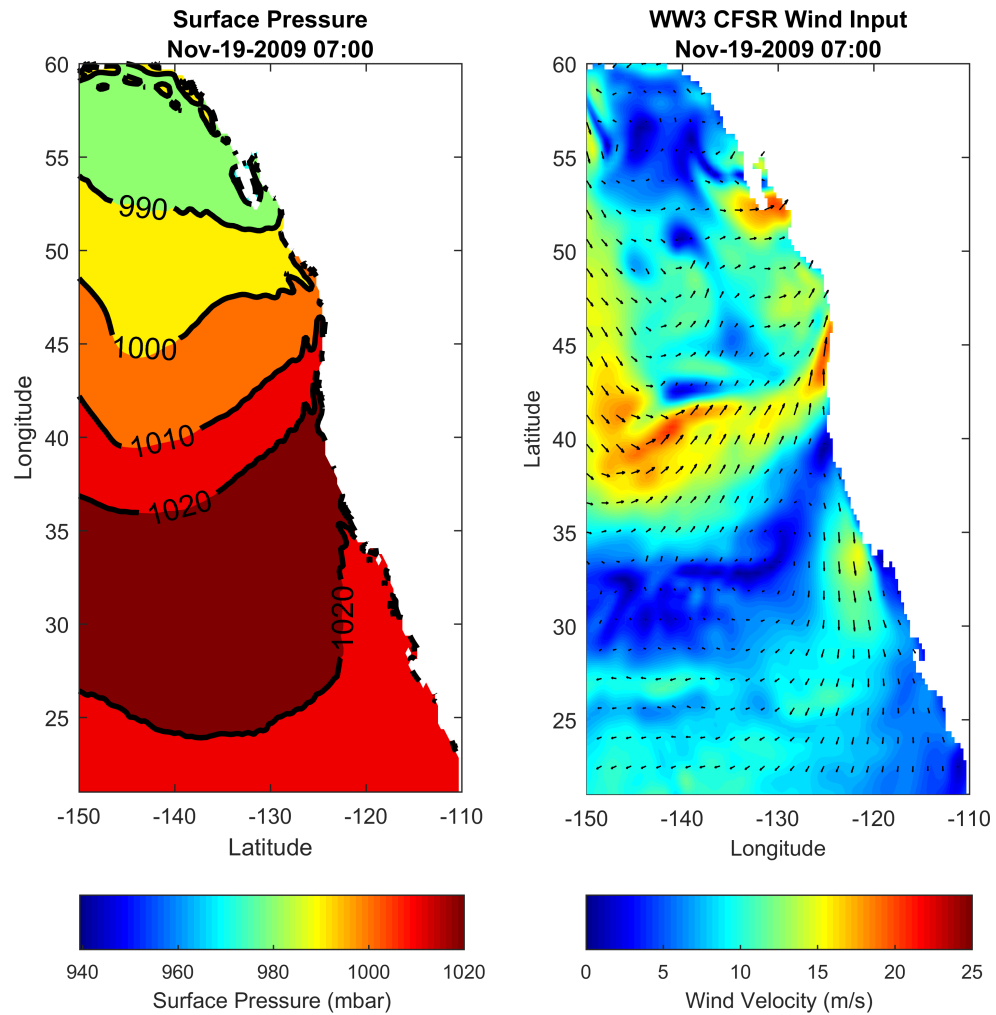
Figure 1.4: The surface pressure and 10 m wind forcing during the peak H_s hour of Event 2. The colors are wind magnitude and contours are pressure in mb.
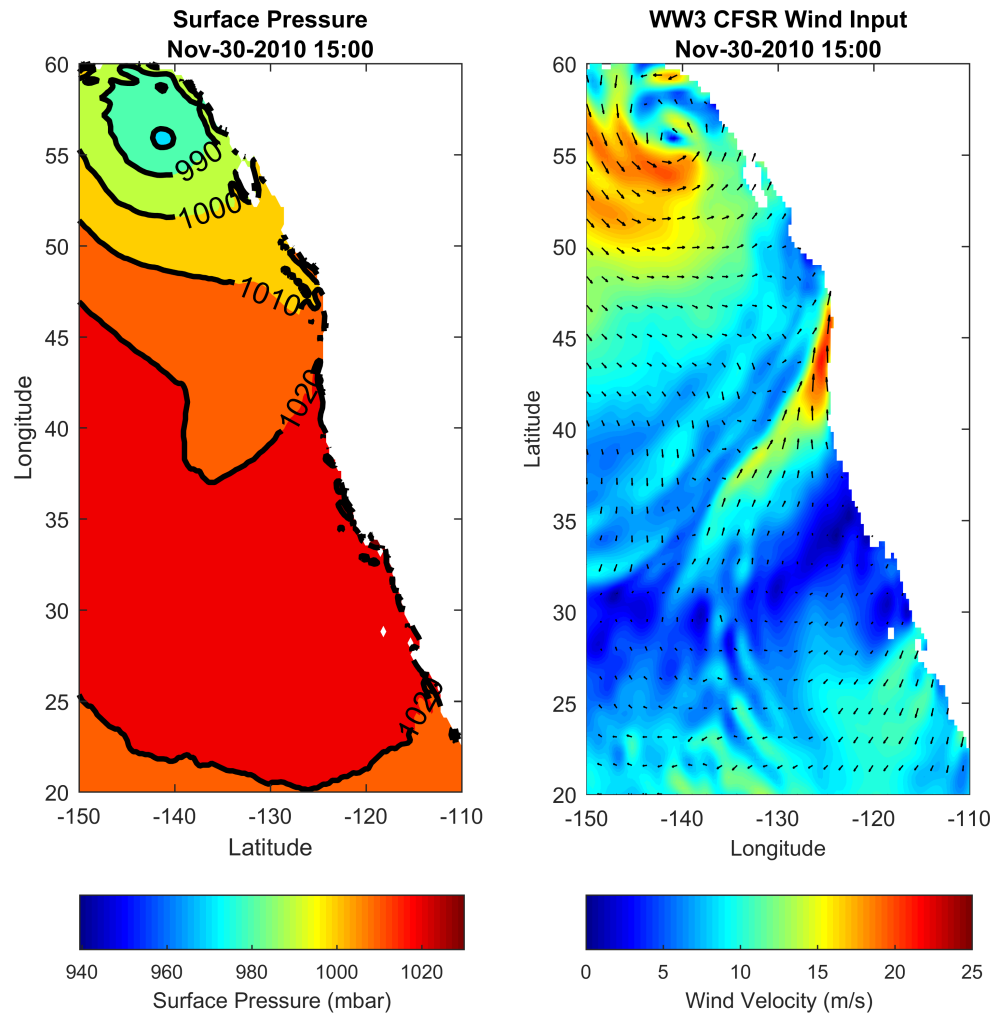
Figure 1.5: The surface pressure and 10 m wind forcing during the peak H_s hour of Event 3. The colors are wind magnitude and contours are pressure in mb.

Chapter 2   Materials and Methods

A spectral model was implemented to assess the wave climatology for the coastlines of southeast Washington and Oregon by producing a seven year hindcast [8] with WaveWatch III. WaveWatch III (WWIII) is a spectral wave model which uses the spectral action balance equation to simulate wave energy propagation along a grid. The application of WWIII to the PNW coastline of [8] involves three nested grids of increasing resolution. The first grid spans the entire Pacific Ocean at a 30 arc-minute resolution, the second the Eastern North Pacific at a 7.5 arc-minute, and the third the continental shelf ($40.3°$ to $49.5°$N $233°$ to $236.25°$W) at a 90 s resolution. The first two outer grids utilize bathymetry from the National Geophysical Data Center's ETOPO1 dataset, and the innermost bathymetry is a blend of the ETOPO1 and NOAA's Gridded Tsunami Bathymetry (Amante et al 2009; Carignan et al 2009; Gorthe et al 2010; Gorthe et al 2011). In direction, the resolution is $10°$. In frequency, the resolution begins at 0.003 Hz for the lowest frequency of 0.03 Hz, and increases to 0.11 Hz for the highest frequencies (1.23 Hz is the highest frequency considered).

The simulation implements the ST2 physics package and is forced every 3 hours by Global Forecasting System (GFS) 10 m winds and air/sea temperature differences. This model configuration will hereafter be referred to as the original model and labeled ST2-GFS to indicate the applicable combination of physics package

and wind input. Generally, the wind input is the first component to be considered to improve wave model results, since the quality of wave model output is directly related to the quality of wind input. Herein, we consider the reanalyzed Climate Forecast System (CFSR) wind product by NCEP. We also implement a newer physics package with source terms from Ardhuin et al (2010) associated with WaveWatch III v. 4.18, referred to as ST4. Recent literature suggests that this package better represents wind/wave and wave/wave energy transfer, thus producing more accurate wave model results [2]. The model configurations implemented in this study are detailed in Table 2.1.

2.1 Wind Input

The two wind input datasets to be compared are the National Center for Environmental Prediction's (NCEP) GFS and the CFSR products. The GFS wind data has a three-hour time resolution, a 0.5° x 0.5° spatial resolution and is used in the original model configuration. In comparison, the CFSR dataset is a reanalyzed product, and therefore benefits from the availability of observations to increase model skill. Further, it is resolved more finely in time and space, at an hourly time resolution and 0.312° x 0.312° spatial resolution. It is a reanalyzed product in which NCEP considered coupled oceanic and atmospheric processes, included a sea ice model in its analysis, and integrated interpolated satellite radiance data into the time series [17]. Studies have found that the CFSR tends to overestimate wind speeds and underestimate wind speeds in the 99th percentile and higher ($\geq$15

m/s) in the Northeast Pacific [19].

2.2 Physics Packages

The ST2 physics package is the original package in WWIII version 4.18, and the ST4 physics package is a new option associated with this version. The ST2 physics package includes the Tolman and Chalikov (1996) source term, which dissipates low and high frequency energy differently by using two distinct dissipation terms. At the highest frequencies, a spectral roll off of f^{-5} is imposed. The source term also utilizes the wind/wave interaction formulation as proposed by Chalikov et al (1993). In contrast, the ST4 physics package combines short and long wave dissipation. This formulation is comprised of an explicit swell dissipation parametrization and cumulative dissipation which captures the energy transfer between short and long waves. It also prescribes different dissipation rates for waves travelling in different directions. It does not impose a spectral roll off for the highest frequencies, but a general shape of $f^{-4.5}$ occurs naturally in this region of the frequency spectrum [20, 2]. The atmospheric source term considers both momentum flux into and out of the wave field as separate physical processes, as opposed to the ST2 physics package, which allows for negative values of the input term. Validation of the ST4 physics package by Ardhuin et al (2010) found a general overestimation of low-frequency energy and a directional spectrum that was generally broader than that which was observed. The ST2 physics package tends to underestimate energy input into the spectrum by the wind for growing seas, which results in an overall

underestimation of wave energy [2, 11, 3].

Table 2.1: Model Configurations

Model Name	Physics Package	Wind		
		Product	Time Resolution	Spatial Resolution
ST2-GFS	ST2	GFS	3 hr	0.5°
ST2-CFSR	ST2	CFSR	1 hr	0.312°
ST4-GFS	ST4	GFS	3 hr	0.5°
ST4-CFSR	ST4	CFSR	1 hr	0.312°

Chapter 3   Results

The three events, selected for featuring the coastal jet and wave heights greater than 6 m, were simulated with the model configurations described in Section 2. The bulk parameter (H_s, T_m, MWD) and spectral output of the models will be compared to observations from NDBC buoy 46050 (see Figure 1.2) using error metrics RMSE, bias and percent error, as defined in Garcia et al (2014) [8]. For this error analysis, data from the three events are combined, and model performance for $H_s \geq 6$ m or $H_s < 6$ m is analyzed to quantify error for the larger wave heights versus the smaller wave heights.

Subsequently, we compare the evolution of the wave energy spectra from each model configuration to that of the buoy. In order to summarize the evolution of the spectra and focus on the energy from the south that is produced by the southerly jet, the spectra are delineated in direction and the H_s and T_m of each portion is calculated. The spectra are only delineated in direction, and not in frequency, due to the broad range of frequencies which can be associated with waves generated by the coastal jet.

3.1 Model Performance: Bulk Parameters

The H_s time series output of each model configuration for each event is presented
in Figure 3.1. The differences between the output of the model configurations
are in the timing and magnitude of the peak H_s. For all time series, ST2-GFS
yields the lowest peak H_s values, while configurations ST2-CFSR, ST4-GFS and
ST4-CFSR yield successively greater magnitudes of H_s (see Figure 3.1).
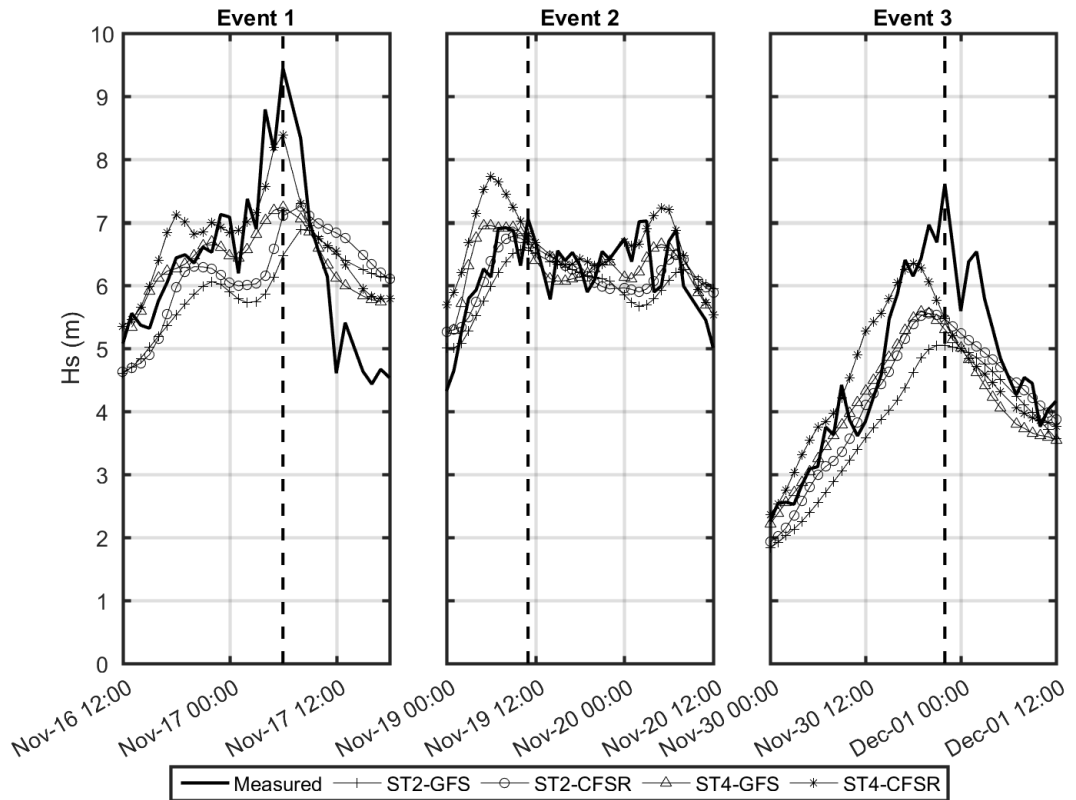

Figure 3.1: Time Series of H_s of each model configuration. The vertical dashed
line corresponds to the peak of the event and the time of the spectrum presented
in the following section

For Event 1, the original model estimates the peak H_s to occur several hours

after, and several meters below, the observed peak. When the CFSR wind is utilized with the original physics package (ST2-CFSR), the peak H_s value increases, but the temporal delay is still present. Elimination of the delay occurs with the implementation of the ST4 physics package and original wind product in ST4-GFS, but the peak H_s is still underestimated. The combination of CFSR wind and ST4 physics package in the ST4-CFSR model configuration both eliminates the delay and increases the peak H_s magnitude, although still ultimately underestimates the peak by approximately one meter.

For Event 2, the original model output has similar temporal delay and under-estimation issues. These issues are ameliorated by the other model configurations; however, in contrast with Event 1, the H_s values are overestimated by ST4-CFSR. For Event 3, the original model output does not have the timing delay seen in Events 1 and 2, but underestimation of H_s occurs by two meters. While the peak wave height is better estimated by the other model configurations, the timing of the peak H_s actually becomes more inaccurate. These model configurations predict the peak to occur before it actually does. Ultimately, the ST4-CFSR model configuration predicts the greatest magnitude peak H_s, but predicts it to occur several hours before the observed peak H_s.

Error statistics RMSE, PE and bias are calculated for H_s, MWD and T_m, as shown in Figure 3.2. For $H_s \geq 6$ m, error statistics decrease with the CFSR wind package and the ST4 physics package (see Figure 3.2).

Specifically, RMSE decreases from 0.92 to 0.68 m between ST2-GFS and ST4-CFSR and bias decreases from -0.3 m to -0.14 m. For MWD of $H_s \geq 6$ m, the
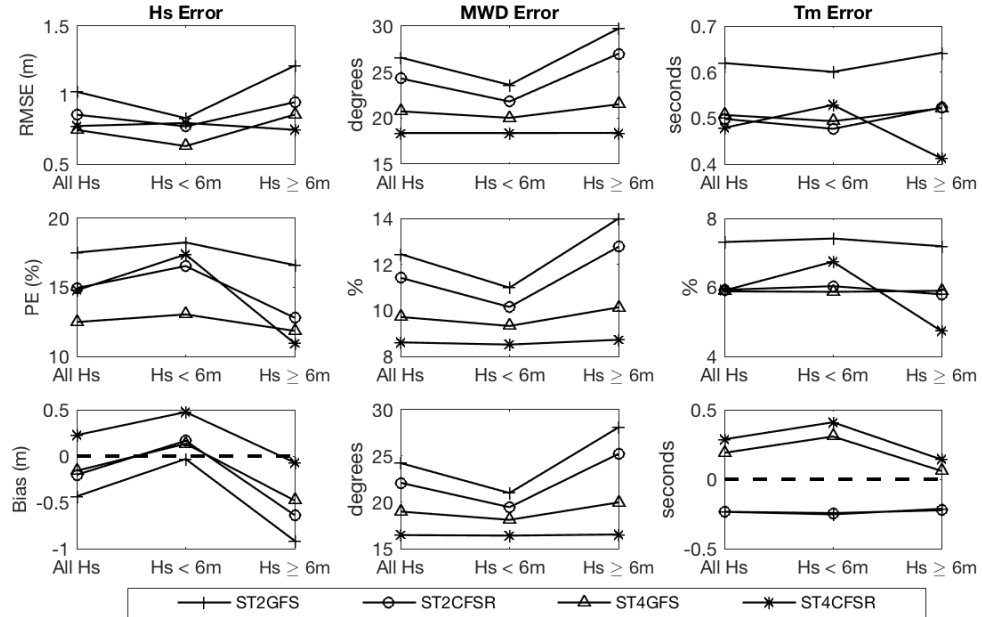
Figure 3.2: Error Statistics RMSE, PE and Bias divided by wave height.

ST4 model configurations perform better than the ST2 model configurations, and ST4-CFSR performs best. MWD bias for all models is positive, indicating that it is estimated to be more northerly than what the buoy reports. For T_m for $H_s \geq 6$ m, underestimation occurs for the ST2 model configurations, and overestimation occurs for the ST4 model configurations. The greatest error statistics for T_m are associated with the original model configuration, and ST4-CFSR renders the smallest error statistics for T_m.

3.2 Model Performance: Energy Spectra

The spectra at the time of maximum wave height for each event are illustrated in Figure 3.3. The spectra reproduced in this figure are those of the original model configuration (ST2-GFS) the model configuration which performs best for the largest wave heights (ST4-CFSR) and as observed by NDBC buoy 46050. Each spectrum is delineated at 120° and then again at either 260° (for Events 1 and 3) or 240° (for Event 2), as illustrated in Figure 3.3. We selected the second limit, 260° or 240°, after inspecting hourly snapshots of each spectrum and subjectively determining the delineating direction which best bounds discrete peaks in the spectrum, especially when multiple peaks are present. The first region, 0°-120°, entails energy traveling away from land. The second region, 120°-240° or 260°, represents energy traveling from the south, or "southern" energy, while the third region, 240° or 260° - 360° represents energy traveling from the north, or "northern" energy.

Generally, the spectra associated with the buoy are spread in direction more severely than the spectra associated with the models. This is a repercussion of the directional distribution function implemented by NDBC in the 2-D wave spectra analysis. The broad directional spread can at times cause the energy associated with the northwest quadrant to 'leak' into the southwest quadrant, and no one limit in direction can be determined to avoid this issue altogether. At each time step, an H_s is computed from the southern and northern quadrants. The time series of the partitioned H_s and T_m are then compared.

The observed spectra, illustrated in Figure 3.3 (right column), show incident wave energy primarily from the south for Events 1 and 3, and split between the north and south for Event 2. This is consistent with the strong influence of the southerly coastal jet in Events 1 and 3. In contrast, the coastal jet is less dominant during Event 2 (see Table 1.1).

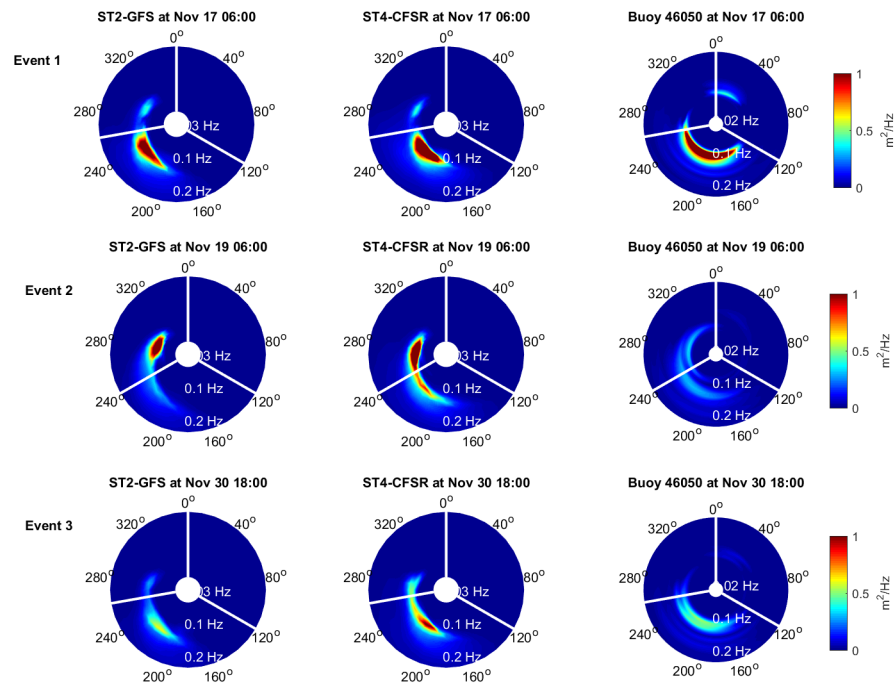Figure 3.3: Example spectra from ST2-GFS, ST4-CFSR and NDBC buoy 46050 at the peak of each event. The radial axis is frequency from 0 to 0.2 Hz. Note the observed southern energy at the buoy as compared to this energy as reproduced by ST4-CFSR and ST2-GFS. The directions at which the spectra are delineated are highlighted in white.

The model-generated spectra generally reproduce the primary peak for Events

1 and 3, but predict a more energetic northern peak for Event 2. For Event 1, the model spectra largely agree with the observed spectrum with the greatest concentration of energy in the southern quadrant. Both model configurations also indicate traces of northern wave energy that do not appear in the observed spectrum. For Event 2, the peaks of the observed spectrum occur at different frequencies, with the southern peak at a higher frequency than the northern peak. While the modelled spectral peaks are also associated with slightly different frequencies, the northern peak is of much greater intensity than the southern peak. For Event 3, the observed spectrum is uni-modal, with the entire peak in the southern quadrant. In contrast, the modelled spectra are bi-modal with energy from both the northern and southern quadrants. These peaks are close in direction and of similar frequency. In each case, ST4-CFSR allocates more energy in the southern quadrant, which is associated with energy from the coastal jet, than ST2-GFS.

The spectra analyzed so far represent only one spectral shape for one hour within the evolution of the event. The energy spectrum can gain intensity in different parts of the spectrum throughout the event, illustrating the changing character of the wave field. This evolution is summarized by the delineated H_s and T_m time series, shown in Figure 3.4. The observations of the buoy show that for all three events, the southern H_s reaches larger values than the northern H_s. Event 2 differs from Events 1 and 3 in that the maximum H_s values associated with the northern and southern peaks are more similar (4 m and 5.5 m for northern and southern H_s, respectively). The southern T_m begins at smaller values for Events 1 and 2, then increases to reach similar values as the northern T_m. This is consistent

with the notion that southern energy is derived from a local wind feature (the jet) which has generated a shorter period sea state that develops into a mid-period swell. In contrast, the northern wave energy is derived from a distant cyclone which has generated mid-period swell.

The differing model configurations produce similar predictions for the northern H_s and T_m that consistently overestimate the observed values by similar amounts for the three events. In contrast, the southern H_s values are underestimated in such a way that the individual model configurations produce more differing results. In other words, the variance of the bias is greater for the southern H_s than the northern H_s. This means that the error for the northern H_s does not become reduced significantly between model configurations, while the error for the southern H_s does become reduced between model configuration output. The original model configuration most severely underestimates the southern H_s and T_m. When the original physics package is combined with the CFSR wind, the magnitude of the southern H_s and T_m increases. These magnitudes increase more when the original wind and ST4 physics package is implemented in ST4-GFS. The final combination of ST4 physics package and CFSR wind yields the most accurate southern H_s and T_m values. This pattern, where each model configuration produces a slightly greater magnitude time series, is seen for each event.

While the magnitude of the overestimation of the northern H_s and T_m is similar between all model configurations, the time at which peak H_s values are reached are slightly different. For Event 2, the time series associated with the ST4 model configurations reach higher energy values before the time series of the ST2 model

configurations. For Event 3, akin to the overall bulk parameter time series trends, ST4-CFSR estimates its peak northern and southern H_s value several hours before the other model configurations estimate their peak H_s values.
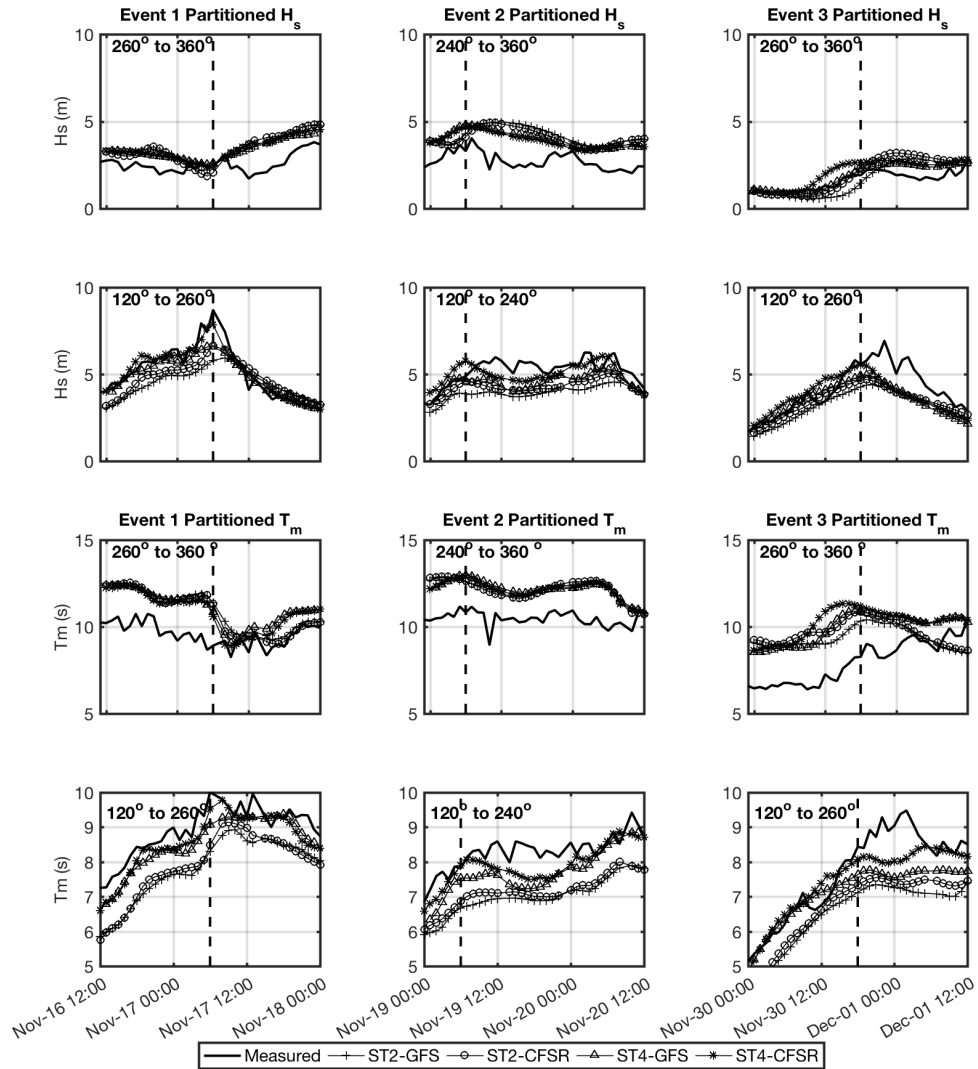
Figure 3.4: H_s and T_m time series calculated from spectra partitioned in the southern quadrant and northern quadrant. The vertical dashed lines indicate the time of the spectral illustrations above. The underestimation of southern energy and overestimation of northern energy is apparent in the H_s figures. Note the different y-axes of the T_m time series.

Chapter 4   Discussion

The output of the four model configurations were considered in the above analysis to determine which best captured the effects of the coastal jet and the resulting large wave heights. For $H_s \geq 6$ m, ST4-CFSR clearly outperforms the other model configurations. Herein, we further explore the contributions of the physics package (ST2 versus ST4) and wind product (GFS versus CFSR) to the improvement in the predictions.

4.1   Impact of chosen physics package on predictions

The ST4 model configurations outperform the ST2 model configurations with respect to accurately reproducing the southern wave energy, as described in the earlier section. With the ST4 configuration, the southern wave energy associated with the coastal jet as well as the timing of the maximum wave height are captured more accurately. To explore the differences in how the ST2 and ST4 physics packages operate, spectral difference plots between the two are inspected to see where and how the results of the two physics packages differ. The spectra plotted in Figure 4.1 are from the peak of Event 1. For the same wind product, more energy accumulates in the lower frequencies (and longer periods) for the ST4 spectrum than for the ST2 spectrum (see Figure 4.1). As described above, the southern

T_m is consistently underestimated, and the ST4 configurations better capture the southern T_m time series by predicting a longer T_m. This is consistent with the positive bias seen in the ST4 physics packages as compared with the ST2 physics packages.
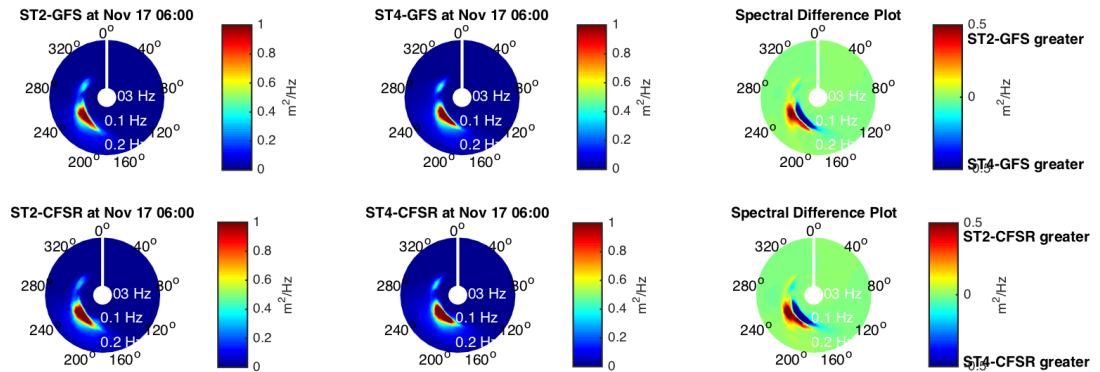
Figure 4.1: The spectra as reproduced by the model configurations which implement the same wind package but ST2 and ST4 physics packages. A difference plot of the two spectra is reproduced in the third column.

4.2   Impact of chosen wind product on predictions

Inspection of model output with respect to wind package reveals that the performance is of better quality when the CFSR wind product is implemented (e.g., ST2-GFS vs ST2-CFSR). The CFSR wind package has an increased temporal and spatial resolution as compared with the GFS wind package (see Table 2.1), and has been reanalyzed with more accurate and detailed physical processes [17]. Cross-sections of the coastal jet associated with each wind package show that the

CFSR wind produces a steep longitudinal gradient which updates hourly to become steeper as the jet tightens. In contrast, the GFS wind cross section reveals a flatter gradient which remains stagnant even as the jet tightens according to the CFSR wind product. The CFSR product also reaches higher wind velocity values.

To explore the relative significance of the spatial or temporal resolution of the wind product on model performance, three variations of ST4-CFSR (hereafter referred to as the "initial" model configuration) are implemented for Event 1. These new configurations include variations in temporal and spatial resolution of wind product. Similar to the analysis performed in Section 3, the respective output is analyzed in terms of bulk parameters and delineated energy spectra.

The first variation, ST4-CFSR-FineGrid, has an increased outermost grid resolution from $0.5°$ to $0.312°$, which matches the resolution of the CFSR wind product. The second variation, ST4-CFSR-CoarseWind, implements a coarser spatial wind input resolution from $0.312°$ to $1.9°$ grid resolution. Note that this spatial resolution is even coarser than that of the GFS wind product. The third variation, ST4-CFSR-3hrWind has a decreased temporal resolution of wind from hourly input to three hour input. This case matches the temporal resolution of the GFS wind product and the spatial resolution of the model runs using the GFS winds. The details of these variations are recorded in Table 4.1.

The output H_s time series for Event 1 for the variations of ST4-CFSR are plotted in Figure 4.2. Severe underestimation occurs with the spatially coarse wind (ST4-CFSR-CoarseWind). The best performance occurs with the highest resolved grid (ST4-CFSR-FineGrid). Specifically, the results for ST4-CFSR-FineGrid are

Table 4.1: Variations of ST4-CFSR

Model Name	Outer Grid Resolution	Wind	
		Time Resolution	Spatial Resolution
ST4-CFSR-FineGrid	0.312°	1 hr	0.312°
ST4-CFSR-3hrWind	0.5°	3 hr	0.312°
ST4-CFSR-CoarseWind	0.5°	1 hr	1.9°

essentially identical to the initial model configuration (ST4-CFSR) with nearly similar RMSE for $H_s \geq 6$ m (approximately 0.67 m, see Figure 4.3).

The significantly decreased performance for the larger wave heights for ST4-CFSR-CoarseWind (RMSE increases from 0.68 to 2 m) occurs despite the fact that this simulation implements the higher quality CFSR wind, but on a much coarser grid. The original wind product, GFS, in this case actually outperforms ST4-CFSR-CoarseWind in predicting wave height. The peak wave height of the output of the third variation, ST4-CFSR-3hrWind, underestimates the initial model peak wave height by approximately 0.5 m, but the RMSE associated with the 3hrWind output is not significantly worse than ST4-CFSR with the 1hrWind output for $H_s \geq 6$ m. This is because the underestimation error at the peak is compensated for by the reduction in overestimation during the beginning of the event. Note that ST4-CFSR-3hrWind performs significantly better than ST4-GFS despite the fact that they both have the same temporal resolution.

When spectral analysis is performed via delineation (as described in Section
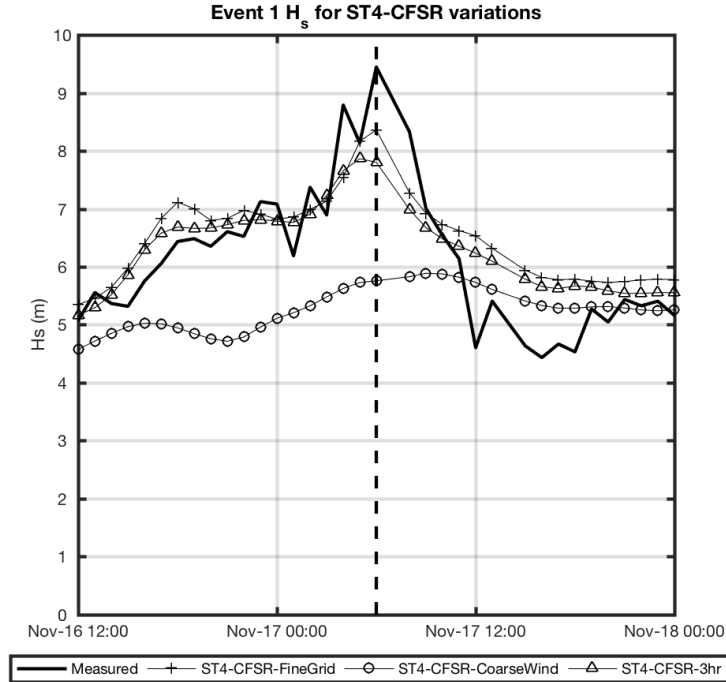
Figure 4.2: Time series of ST4-CFSR variations. The initial model configuration, ST4-CFSR, is not plotted because it overlays over ST4-CFSR-FineGrid such that the differences cannot be seen by eye.

3b), and partitioned H_s and T_m are calculated, the trends between the northern and southern H_s time series with respect to the buoy are similar to the initial ST4-CFSR configuration (see Figure 4.4). The northern H_s and T_m are overestimated by all variations by a similar magnitude. Specifically, the northern T_m is overestimated until the event peak, at which point it more closely follows the observed northern T_m. The overestimation during the first part of the time series suggests that the model predicts a more developed wave field (with longer period) than was observed. In contrast, the southern H_s and T_m are underestimated. The southern H_s underestimation is most severe for ST4-CFSR-CoarseWind, and
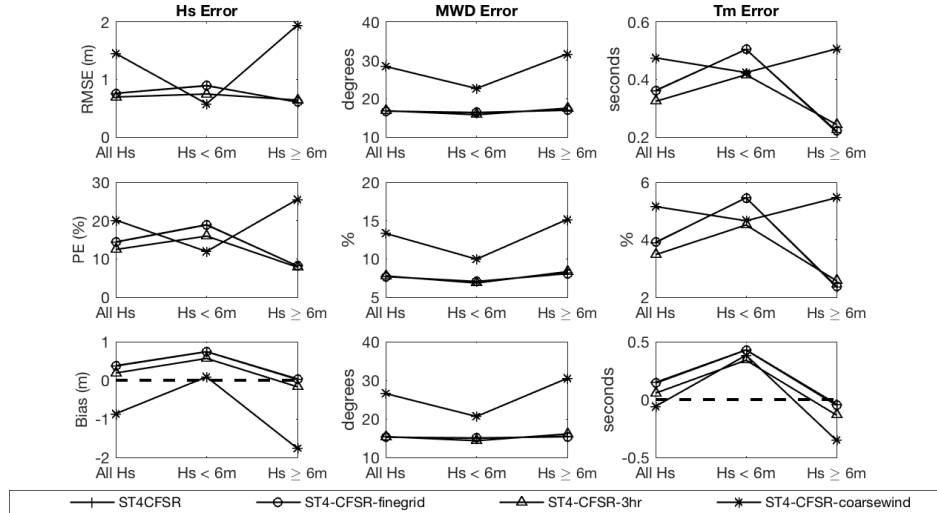
Figure 4.3: Error statistics RMSE, PE and Bias binned by Wave Height for the ST4 model variations.

least severe for ST4-CFSR-FineGrid. ST4-CFSR-3hrWind most closely follows the southern H_s time series as measured by the buoy, but still underestimates the maximum wave height by 1 m. The southern T_m is underestimated most severely by ST4-CFSR-CoarseWind, but underestimation also occurs for ST4-CFSR-FineGrid. These underestimations reveal that the overall effect of the atmospheric forcing in producing a more developed southern wave field is not completely reproduced.

Overall, the factor which most significantly affects the model performance is the spatial resolution of the wind, as seen by the worse performance of ST4-CFSR-CoarseWind. This signifies that the spatial detail of the atmospheric forcing is important in the model physics. In contrast, the decrease in temporal resolution from 1 hour to 3 hours does not affect the model results significantly as long as the wind field is highly spatially resolved. These findings suggest that a wind product
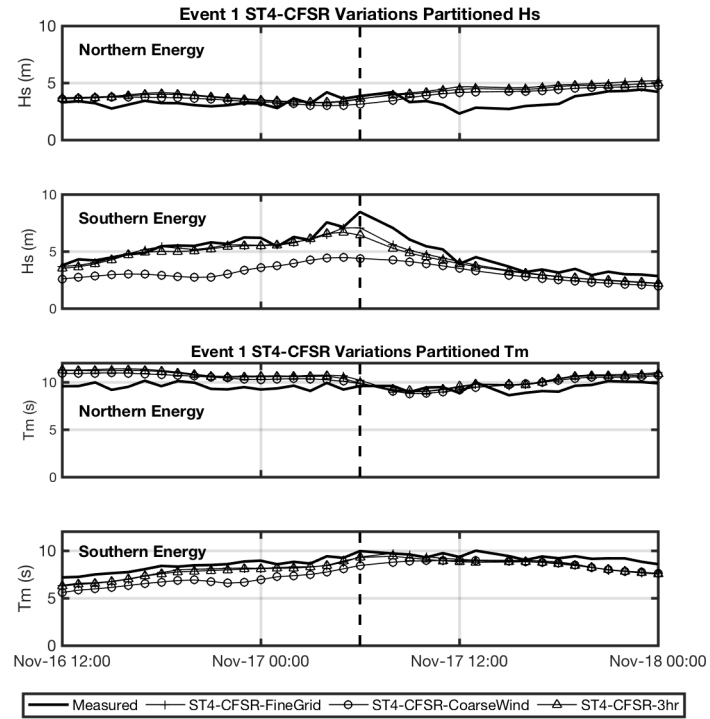
Figure 4.4: Time Series of Partitioned H_s and T_m for the ST4-CFSR variations.

that represents the fine spatial details of the coastal jet is crucial for accurate prediction of the southern wave energy.

Chapter 5 Conclusions

Understanding how large waves are generated can help to mitigate risk associated with them. The northeast Pacific is an optimal location to study such events, as large wave events occur frequently in this area. This study aimed to understand how current models fail to capture the peak wave height of such events by simulating historical storms for which models have underperformed.

Three large wave events, wherein H_s exceeds 6 m for longer than 5 hrs, were simulated. The time series of each event is represented in Figure 1.5. The H_s time series of Events 1 and 3 rises and declines rapidly, and the H_s time series of Event 2 remains relatively constant throughout the event. The atmospheric conditions which generate these events include a wind feature called a coastal jet along with a distant cyclone. Events 1 and 3 feature the coastal jet at all times while the coastal jet is more fleeting, of less intensity and of smaller latitudinal extent in Event 2. Also, Events 1 and 3 are characterized by a strong wave energy signal from the southwest, while Event 2 wave energy is divided more equally between waves incident from the northwest and southwest. To explore the importance of various inputs on model performance in simulating these events, different combinations of physics package and wind forcing (Table 2.1) were utilized in the simulations.

Overall, the combination of ST4 physics package and the CFSR winds combination yielded the lowest error statistics for bulk parameters H_s, MWD and T_m

for data points associated with $H_s \geq 6$ m. For these data points, ST4-CFSR reduced RMSE for wave height, direction, and period, by approximately 0.5 m, 12° and 0.3 s, respectively. However, the output still underestimates peak H_s, overestimates MWD and underestimates T_m. The peak H_s value of the ST4 model configurations occurs at a similar time as the peak observed H_s for Events 1 and 2, while the ST2 configurations result in a peak wave height which occurs after the observed peak wave height. For Event 3, however, the ST4 configurations predict the peak H_s value to occur before the peak observed H_s.

We also explored the importance of the resolution of these inputs in model performance by changing their resolution and simulating Event 1. We found that increasing the spatial resolution of the grid did not render better model performance, but a decrease of spatial resolution of wind input (0.5° to 1.9°) severely decreased model performance. In fact, the spatially coarser wind input affects model performance more severely than a temporally coarser wind input. This signifies that accurately modelling the wave energy generated by the jet is sensitive to resolving the fine physical details of the jet as opposed to the temporal variability over time scales shorter than 3 hours.

Analysis of the energy spectra included delineation of the spectra into northern and southern quadrants and calculation of the partitioned H_s and T_m. These partitioned bulk parameters were compared with the observed partitioned bulk parameters. The partitioned H_s and T_m showed that the wave energy from the southwest is stronger, and of shorter period, than the wave energy from the northwest. The model configurations tend to underestimate H_s and T_m associated with

energy from the southwest, and overestimate H_s and T_m associated with the wave energy from the northwest. The original model, ST2-GFS, produces output which most severely underestimates and overestimates energy from the southwest and northwest, respectively. The ST4 configurations output more accurate representations of the larger H_s and longer T_m values associated with wave energy from the southwest. This could be due to the ST4 physics package allocating more energy into the lower frequencies as compared to the ST2 configurations. The combination of ST4 physics package with the CFSR wind product, ST4-CFSR, yields the best representation of the energy from the southwest among the four model configurations. However, the wave energy from the northwest was overestimated by this model configuration by a similar magnitude as the other configurations. The combination of over and under estimations of the energy from the northern and southern quadrants, respectively, results in a relatively accurate bulk parameter.

Bibliography

[1] Jonathan Allan and Paul Komar. "Are ocean wave heights increasing in the eastern North Pacific?" In: *Eos, Trans. Amer. Geophys. Union* 81.47 (2000), pp. 561–567.

[2] Fabrice Ardhuin et al. "Semiempirical dissipation source functions for ocean waves. Part I: Definition, calibration, and validation". In: *J. Phys. Oceanogr.* 40.9 (2010), pp. 1917–1941. DOI: 10.1175/2010JPO4324.1.

[3] Fabrice Ardhuin et al. "Swell and slanting-fetch effects on wind wave growth". In: *Journal of Physical Oceanography* 37.4 (2007), pp. 908–931.

[4] Arno Behrens and Heinz Günther. "Operational wave prediction of extreme storms in Northern Europe". In: *Natural Hazards* 49.2 (2009), pp. 387–399. DOI: 10.1007/s11069-008-9298-3.

[5] Steven Businger, Selen Yildiz, and Thomas E Robinson. "The Impact of Hurricane Force Wind Fields on the North Pacific Ocean Environment". In: *Weather and Forecasting* 30.3 (2015), pp. 742–753.

[6] Luigi Cavaleri. "Wave modeling-missing the peaks". In: *J. of Phys. Oceanogr.* 39.11 (2009), pp. 2757–2778.

[7] James D Doyle. "The influence of mesoscale orography on a coastal jet and rainband". In: *Mon. Wea. Rev.* 125.7 (1997), pp. 1465–1488. DOI: `10.1175/1520-0493(1997)125<1465:TIOMOO>2.0.CO;2`.

[8] Gabriel García-Medina, H Tuba Özkan-Haller, and Peter Ruggiero. "Wave resource assessment in Oregon and southwest Washington, USA". In: *Renewable Energy* 64 (2014), pp. 203–214.

[9] Nicholas E Graham and Henry F Diaz. "Evidence for intensification of North Pacific winter cyclones since 1948". In: *Bull. Amer. Meteor. Soc.* 82.9 (2001), pp. 1869–1893. DOI: `10.1175/1520-0477(2001)082<1869:EFIONP>2.3.CO;2`.

[10] John R Gyakum et al. "North Pacific cold-season surface cyclone activity: 1975-1983". In: *Mon. Wea. Rev.* 117.6 (1989), pp. 1141–1155.

[11] Mohammad Hossein Kazeminezhad and Seyed Mostafa Siadatmousavi. "Performance evaluation of WAVEWATCH III model in the Persian Gulf using different wind resources". In: *Ocean Dynamics* (2017), pp. 1–17.

[12] Paul D Komar and Jonathan Allan. *Analyses of extreme waves and water levels on the Pacific Northwest coast.* Oregon Department of Land Conservation and Development, 2000.

[13] S Ponce de León and C Guedes Soares. "Extreme wave parameters under North Atlantic extratropical cyclones". In: *Ocean Modelling* 81 (2014), pp. 78–88.

[14] Sonia Ponce de León, João H Bettencourt, and Frederic Dias. "Comparison of numerical hindcasted severe waves with Doppler radar measurements in the North Sea". In: *Ocean Dynamics* 67.1 (2017), pp. 103–115. DOI: `10.1007/s10236-016-1014-3`.

[15] Melisa Menéndez et al. "Variability of extreme wave heights in the northeast Pacific Ocean based on buoy measurements". In: *Geophysical Research Letters* 35.22 (2008).

[16] Peter Ruggiero, Paul D Komar, and Jonathan C Allan. "Increasing wave heights and extreme value projections: The wave climate of the US Pacific Northwest". In: *Coastal Engineering* 57.5 (2010), pp. 539–552. DOI: `10.1016/j.coastaleng.2009.12.005`.

[17] Suranjana Saha et al. "The NCEP climate forecast system reanalysis". In: *Bull. Amer. Meteor. Soc.* 91.8 (2010), p. 1015.

[18] Richard J Seymour. "Evidence for changes to the northeast Pacific wave climate". In: *J. Coast. Res.* 27.1 (2011), pp. 194–201. DOI: `10.2112/JCOASTRES-D-09-00149.1`.

[19] Justin E Stopa and Kwok Fai Cheung. "Intercomparison of wind and wave data from the ECMWF Reanalysis Interim and the NCEP Climate Forecast System Reanalysis". In: *Ocean Modelling* 75 (2014), pp. 65–83.

[20] Justin E Stopa et al. "Comparison and validation of physical wave parameterizations in spectral wave models". In: *Ocean Modelling* 103 (2016), pp. 2–17. DOI: `10.1016/j.ocemod.2015.09.003`.

APPENDIX

Chapter A   Error Statistics: All Data

This analysis summarizes the performance of a hindcasted data set discussed in Garcia et al (2014) [8]. The hindcast spans the years 2005-2011. Bulk parameters of significant wave height and energy period are compared to measured bulk parameters. A depiction of an overall scatter plot for the full dataset (N=24,695 data points) is presented in Figure A1. The greatest number of data points occur for $H_s \geq 6$ m. Statistical values quantifying the comparison include root-mean-squared-error (RMSE), percent error (PE), bias, scatter index (SI) are defined as follows, where N, MEAS and EST are the total number of output points, measured and modeled values, respectively.:

$$RMSE = \sqrt{\frac{\sum \left(MEAS - EST\right)^2}{N}} \tag{A.1}$$

$$PE = 100\sqrt{\frac{1}{N} \sum \left(\frac{MEAS - EST}{MEAS}\right)^2} \tag{A.2}$$

$$SI = \frac{RMSE}{MEAS} \tag{A.3}$$

$$Bias = \frac{1}{N} \sum EST - MEAS \tag{A.4}$$

The overall RMSE for H_s is 0.50 m, PE is 20%, SI is 0.20 and bias is positive at 0.11 m.
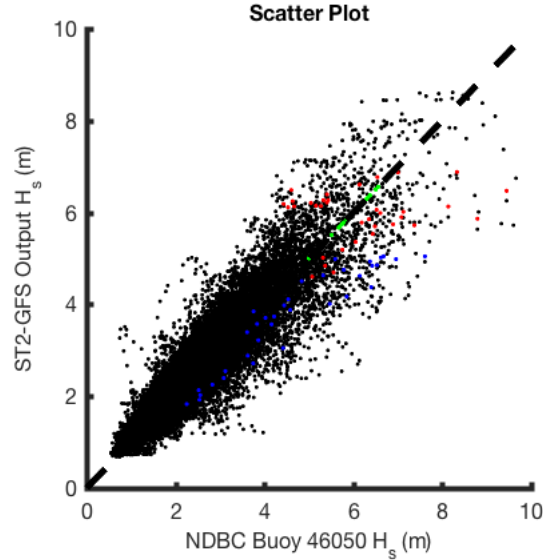
Figure A.1: Scatter Plot, all data points for all years of model hindcast (2005-2011). The colored points are the cases considered in this study, where Events 1, 2, and 3 are colored red, green, and blue, respectively.

A.1   Error Statistics: Binned by Wave Height

To gain an intuition of statistical trends for wave heights of interest, the data is divided into regions of wave heights greater than 6 m, between 4 and 6 m, and less than 4 m. Wave height error statistics are summarized in the Table A1.

Table A.1: Error Statistics Binned by Wave Height

Wave Heights (m)	N (-)	RMSE (m)	PE (%)	Bias (m)	SI (-)
<4	21944	0.42	20	0.14	0.2
4-6	2412	0.81	17	-0.03	0.17
≥6	339	1.34	19	-0.67	0.2
Overall	**24695**	**0.5**	**20**	**0.11**	**0.2**

RMSE and bias increase as the wave heights increase. RMSE and bias are significantly greater for data associated with the larger significant wave height, although PE and SI do not demonstrate a significant increase between the smallest and largest wave heights. The model tends to slightly overestimate wave heights less than 4 m (positive bias of 0.14 m), but underestimate wave heights larger than 6 m (negative bias of 0.67 m).

While dividing the data into regions of wave height is helpful to gain a broad understanding of data trends, binning the data into tighter divisions may lend more insight into nuances of the error between different wave heights. This is illustrated in Figure A2, where results are also presented by season to illustrate the differences throughout the year and the associated model performance. Note that there are no data points associated with a wave height of 8.5 m for winter.

RMSE clearly increases with increasing wave height. These elevated levels of RMSE for wave heights greater than 6 m are due primarily to model error for the largest wave heights. PE and SI begin at elevated levels before dropping at 1.5 meter significant wave height to reach minimal values between 3 and 5 m for fall, winter and spring. The elevated levels of PE and SI statistics can be understood as these statistics are normalized by wave height, and the small wave height value thus renders a greater error statistic value for similar absolute errors.

To hone in specifically on the model performance for the greater wave heights and associated energy period dependence, the data is divided into 'smaller' and 'larger' wave height categories (less than 6 m and greater than 6 m), and then binned by energy period. The error statistics are then calculated. The results are
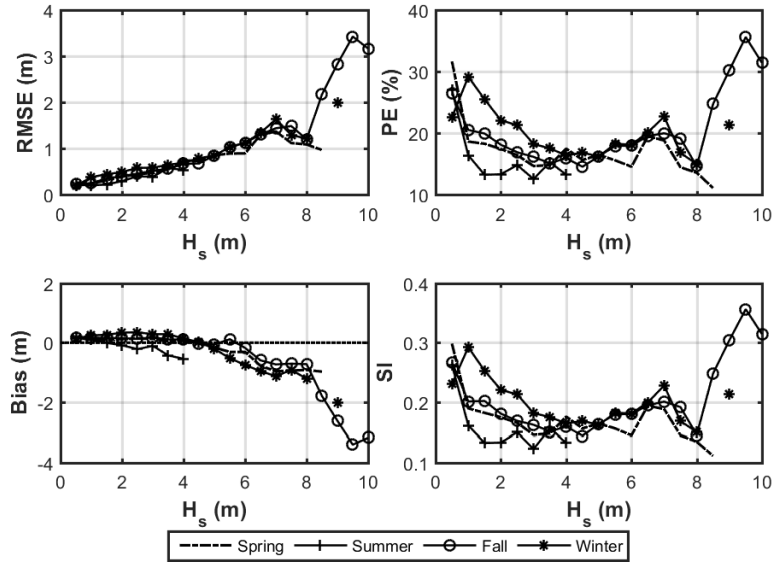
Figure A.2: Error Statistics binned by wave height and divided by season

illustrated in Figure A.3.

Error statistics exhibit a different trend for the larger and smaller wave heights. Overall, greater values are reached for $H_s \geq 6$ m (right panel) than $H_s <$ than 6 m (left panel). The error statistics for the smaller wave heights remain relatively consistent throughout the energy periods until an energy period of about 11 seconds. At this point, error statistic values diverge depending on season.

For the larger wave heights, however, data points have highest error statistic values for either end of the energy period range. The shortest and longest energy periods exhibit the greatest values of SI, PE and RMSE, and the most negative bias. The smallest error statistic values occur for energy periods between 11 and 14 seconds, signifying that mid-period swell is the region of best model performance.

In this region, bias is slightly positive as opposed to negative at either limit of Te values.
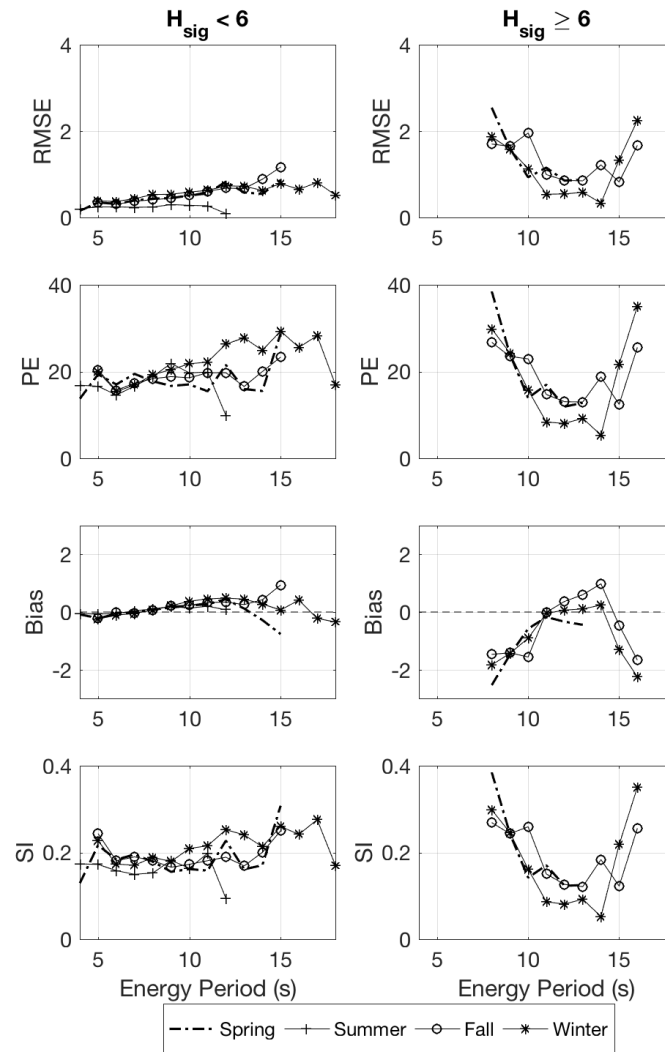
Figure A.3: Error Statistics, data divided by wave height and binned by energy period